Measuring Masses Using Correlations

David Wagner

February 25, 1997

1 Introduction

This document describes several different techniques for measuring masses of supersymmetric particles at the NLC.

1.1 Simulations

For the bulk of this document, we will be concentrating on the following supersymmetric process:

- Selectrons: $e^+e^- \to \tilde{e}_R^+\tilde{e}_R^- \to \tilde{\chi}_1^0 e^+ \tilde{\chi}_1^0 e^-$ at $\sqrt{s} = 500$ GeV

(so we will mostly be talking about those events that have exactly two electrons in the final state with no other activity in the detector). In a few other places, we will discuss two other processes:

- Charginos: $e^+e^- \to \tilde{\chi}_1^+\tilde{\chi}_1^- \to \tilde{\chi}_1^0 q_1 \overline{q}_2 \tilde{\chi}_1^0 \ell^\pm \nu_\ell$ at $\sqrt{s} = 250$ GeV
- Squarks: We are interested in both top squark production ($e^+e^- \to \tilde{t}_1\tilde{t}_1$ with $\tilde{t}_1 \to \tilde{\chi}_1^+ b$ or $\tilde{t}_1 \to \tilde{\chi}_1^0 t$ and $t \to q_1\overline{q}_2 b$) and bottom squark production ($\tilde{b}_1 \to \tilde{\chi}_2^0 b$ or $\tilde{b}_1 \to \tilde{\chi}_1^- t$). We run the NLC at $\sqrt{s} = 600$ GeV so that only third-generation squarks will be produced; we will see how well we can separate the $\tilde{t}_1$ and $\tilde{b}_1$ squarks.

For concreteness, we choose point 3 parameters, which yield $M_{\tilde{\chi}_1^0} = 44.52$ GeV, $M_{\tilde{e}_R^\pm} = 206.54$ GeV, $M_{\tilde{t}_1} = 260.08$ GeV and $M_{\tilde{b}_1} = 278.42$ GeV.

This document uses two Monte Carlo simulations—a fast four-vector generator (with optional smearing of electron energy but no other detector effects included) and a more complete simulation using ISAJET as the generator (version 7.22 for the 250 and 500 GeV data, and version 7.27 for the 600 GeV studies) with a simple detector simulation. In the ISAJET studies, background from W-pair production was also included.

1.2 Event selection

In all cases, we require that there be no energy in the calorimeter at an angle of $|\cos\theta| > 0.90$, which is the region where there is not complete tracking coverage in the current NLC detector design.

For the $\tilde{e}_R^\pm \to \tilde{\chi}_1^0 e^\pm$ studies, we make a cut on the electron energy. This is allowable as long as it does not bias the measurement of E_{min} and E_{max} that we are making. Figure 2a shows the electron energy distribution from both $\tilde{e}_R^\pm$ decays and from background. A cut of 35 GeV and 205 GeV clearly does not affect the endpoints of the distribution for the signal. To the extent that the decays in both hemispheres of the event are uncorrelated, eliminating events with electrons outside the cuts in one hemisphere may eliminate background electrons that are within the cut in the other hemisphere.

For the squark studies, we take the b-tagging efficiency to be 80% with a purity of 97.5%.

2 Endpoint method

2.1 Two-body decays

Consider the process $e^+e^- \to A + A$ with $A \to B + C$. Let Σ' be the rest frame of particle A and Σ be the lab frame. Since the decay of A is a two-body decay, we can write:

$$\begin{aligned} E'_C &= \frac{M_A^2 - M_B^2 + M_C^2}{2M_A} \\ p'_C &= \frac{\left[\left(M_A^2 - (M_C + M_B)^2\right)\left(M_A^2 - (M_C - M_B)^2\right)\right]^{1/2}}{2M_A} \end{aligned} \tag{1}$$

In the case where C is very light (say, an electron), then these equations reduce to:

$$p'_C = E'_C = \frac{M_A^2 - M_B^2}{2M_A}$$

In the CM frame, E'_C is unique; when C is boosted to the lab frame, its energy, E_C, depends on the angle of its decay relative to the direction of A (E_C is maximum when $\mathbf{p}'_C$ is parallel to $\mathbf{p}_A$ and minimum when $\mathbf{p}'_C$ is antiparallel to $\mathbf{p}_A$). E_C will have a flat distribution, with minimum and maximum energy given by:

$$\begin{aligned} E_{C,min} &= \gamma p'_C - \beta\gamma E'_C \\ E_{C,max} &= \gamma p'_C + \beta\gamma E'_C \end{aligned} \tag{2}$$

where

$$\begin{aligned} \gamma &= E_A/M_A \\ \beta\gamma &= p_A/M_A \end{aligned}$$

Figure 1a shows that the electron energies from $\tilde{e}_R^{\pm}$ decays form a box distribution. In the real detector, this will be modified by detector resolution. The current NLC detector design has an electromagnetic energy resolution of

$$\frac{\sigma}{E} = 1\% + \frac{12\%}{\sqrt{E}}, \tag{3}$$

and a hadronic energy resolution of

$$\frac{\sigma}{E} = 2\% + \frac{45\%}{\sqrt{E}}.$$

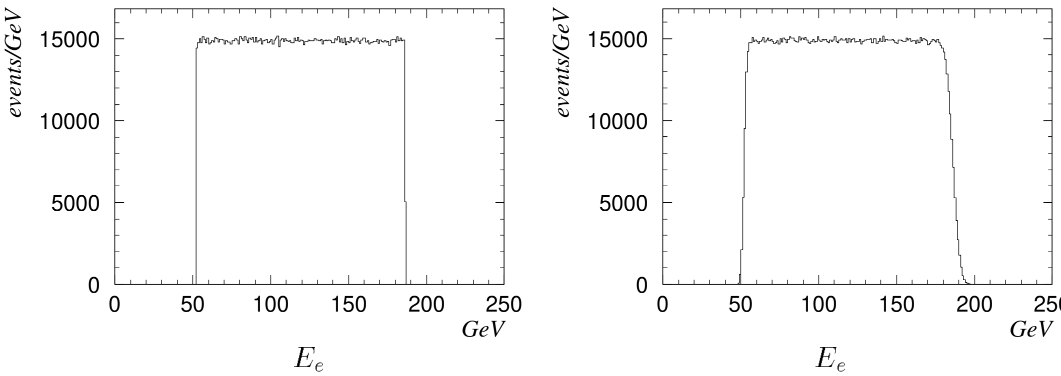

Figure 1: (a) The distribution of true electron energies from 10^6 $\tilde{e}_R^+\tilde{e}_R^-$ events with $\tilde{e}_R^{\pm} \to \tilde{\chi}_1^0 e^{\pm}$. (b) The same distribution, including the electromagnetic calorimeter energy resolution given in Equation 3.

Write the unsmeared electron energy distribution as:

$$f(E) = \begin{cases} 0 & E < E_{min} \\ k & E_{min} < E < E_{max} \\ 0 & E > E_{max} \end{cases}$$

If the detector has a constant energy resolution σ, then the electrons will be distributed according to:

$$\begin{aligned} g(E) &= \int_{-\infty}^{\infty} f(E')e^{-(E-E')^2/2\sigma^2}\,dE' \\ &= \frac{k}{2}\left[\operatorname{erfc}\left(\frac{E-E_{max}}{\sqrt{2}\sigma}\right) - \operatorname{erfc}\left(\frac{E-E_{min}}{\sqrt{2}\sigma}\right)\right] \end{aligned} \tag{4}$$

In the above derivation, we cheated by treating σ as a constant to simplify the integration. If $\sigma(E)$ is small and varies slowly across the distribution, we can just replace σ by $\sigma(E)$ in Equation 4:

$$g(E) = \frac{k}{2}\left[\operatorname{erfc}\left(\frac{E-E_{max}}{\sqrt{2}\sigma(E_{max})}\right) - \operatorname{erfc}\left(\frac{E-E_{min}}{\sqrt{2}\sigma(E_{min})}\right)\right] \tag{5}$$

where $\sigma(E) = 0.01E + 0.12\sqrt{E}$. Figure 1b shows the distribution of data from $\tilde{e}_R^\pm \to \tilde{\chi}_1^0 e^\pm$ decays, including the energy resolution smearing, which is clearly visible.

For the process $e^+e^- \to A + A$, we know that $E_A = E_{beam}$ and $p_A = \sqrt{E_{beam}^2 - M_A^2}$. If B is invisible and has an unknown mass, then we have two unknowns, M_A and M_B, and two observables E_{min} and E_{max}. We can then solve Equations 2 for the masses (assuming C is massless):

$$\begin{aligned} M_A &= \frac{E_{beam}}{2}\left[\frac{E_{max}E_{min}}{(E_{max}+E_{min})^2}\right]^{\frac{1}{2}} \\ M_B &= \frac{E_{beam}}{2}\left[\left(\frac{E_{max}E_{min}}{E_{max}+E_{min}}\right) \times \left(\frac{1}{E_{max}+E_{min}} - \frac{4}{E_{beam}}\right)\right]^{\frac{1}{2}} \end{aligned} \tag{6}$$

For example, in the decay $\tilde{e}_R^+ \to \tilde{\chi}_1^0 e^+$ $E_{e,min} = 52.0$ GeV and $E_{e,max} = 186.4$ GeV. Figure 2a shows a fit to ISAJET data (including backgrounds) to Equation 5, where only E_{min}, E_{max} and the histogram normalization are allowed to float. This fit yields a fitted $E_{min} = 51.2$ GeV and $E_{max} = 186.7$ GeV.

Alternatively, we can loop over values of $M^*_{\tilde{e}_R}$ and $M^*_{\tilde{\chi}_1^0}$, and calculate the corresponding $E^*_{e,min}$ and $E^*_{e,max}$ from Equations 2 and find the masses which best reproduce the measured $E_{e,min}$ and $E_{e,max}$. This may be appropriate when M_C is large enough that the approximations used in deriving Equation 6 are no longer valid. Figure 2b shows the result of this procedure. The errors are probably underestimated in this fit; taking the difference between the true and fit masses as the estimate of the errors, then we have made a 0.5% measurement of the $\tilde{e}_R^\pm$ mass, and a 2% measurement of the $\tilde{\chi}_1^0$ mass.

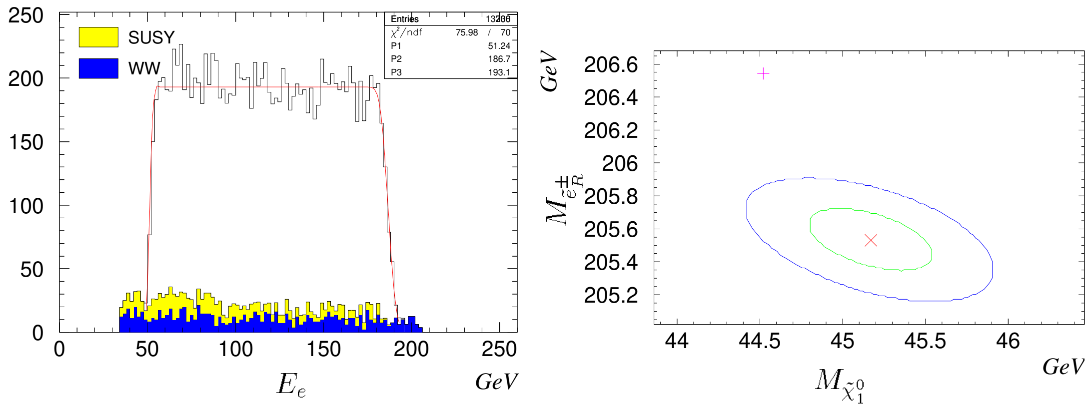

Figure 2: (a) The distribution of electron energies from $\tilde{e}_R^\pm \to \tilde{\chi}_1^0 e^\pm$ decays, as well as backgrounds. The fit is a three-parameter fit to Equation 5 where E_{min}, E_{max} and the histogram normalization are allowed to float but the resolution is required to be $\sigma(E) = 0.01E + 0.12\sqrt{E}$. The fit gives $E_{min} = 51.24$ GeV and $E_{max} = 186.7$ GeV. (b) $M^*_{\tilde{e}_R}$ and $M^*_{\tilde{\chi}_1^0}$ are varied to find the best match to E_{min} and E_{max}.

The $\tilde{e}_R^\pm$ decay is not the best way of determining $M_{\tilde{\chi}_1^0}$; it is much better measured from $\tilde{\chi}_1^\pm$ decays. If we know the mass of the $\tilde{\chi}_1^0$ then we can use it to make a better measurement of $M_{\tilde{e}_R}$. One method is to loop over possible values of $M_{\tilde{e}_R}$, and for each $M^*_{\tilde{e}_R}$, calculate the corresponding E^*_{min} and E^*_{max}; then we try to minimize the quantity

$$\Delta = \sqrt{\frac{(E_{min} - E^*_{min})^2}{(\delta E_{min})^2} + \frac{(E_{max} - E^*_{max})^2}{(\delta E_{max})^2}}. \tag{7}$$

Figure 3 shows this quantity as a function of $\tilde{e}^{\pm}_R$ mass, given the measured values of E_{min} and E_{max} from Figure 2, and setting the mass of the $\tilde{\chi}^0_1$ to be its true mass. The minimum of the distribution is very close to the true $\tilde{e}^{\pm}_R$ mass.

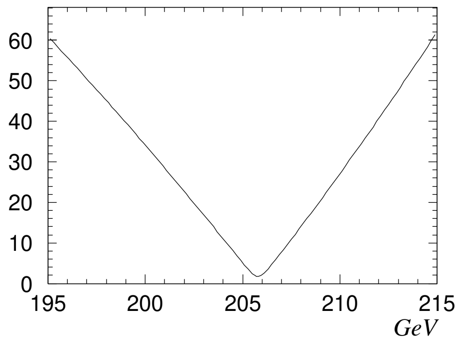

Δ vs $M^*_{\tilde{e}_R}$

Figure 3: The distribution of the quantity Δ from Equation 7.

[The quantity Δ should work out to be some sort of χ^2 quantity. The above plot assumes that there is no error on $M_{\tilde{\chi}^0_1}$.]

2.2 Three-body decays

Now consider the decay $A \to B + C + D$, where B is unknown but C and D can be measured (for example $e^+e^- \to \tilde{\chi}^0_2\tilde{\chi}^0_2$ with $\tilde{\chi}^0_2 \to \tilde{\chi}^0_1 e^+e^-$). In what follows, we construct for every event the invariant mass of C and D, $M_X = \sqrt{(E_C + E_D)^2 - (\mathbf{p}_C + \mathbf{p}_D)^2}$. If we treat M_X as if it were the mass of a true particle (hence $A \to B+X$ with $X \to C+D$), then we treat the decay of X as a two body decay as in section 2.1. For a given value of M_X, the energy $E_X = E_C + E_D$ will be uniformly distributed between some minimum and maximum value.

Figure 4 shows the decays of $\tilde{\chi}^0_2 \to \tilde{\chi}^0_1 e^+e^-$. The sum of the electron energies is not a flat distribution (b); however, by requiring that the invariant mass be in a certain range, the energy sum will be flat (d).

In fact, since each cut on M_{ee} slices the distribution in Figure 4a into statistically independent samples, we can make multiple measurements with the same set of events.

This method is fine when there are enough events to allow narrow cuts in M_X, but in many cases, there won't be enough events. In that case, we could just fit to the entire distribution in Figure 4b without slicing. The endpoints of this distribution is just as predictable. *[I haven't actually looked up the formula or done the integration. However,*

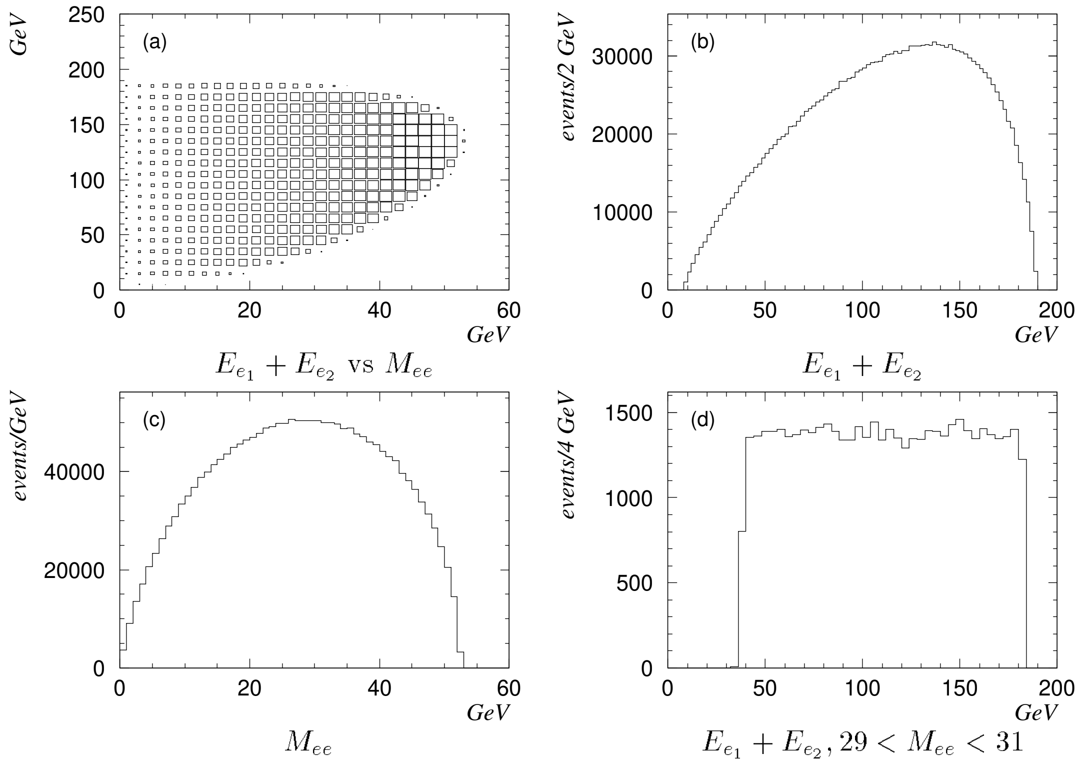

Figure 4: Distributions from a generator-level simulation of 10^6 $\tilde{\chi}_2^0\tilde{\chi}_2^0$ events with $\tilde{\chi}_2^0 \to \tilde{\chi}_1^0 e^+ e^-$. (a) $E_{e_1} + E_{e_2}$ vs M_{ee}. (b) The $E_{e_1} + E_{e_2}$ distribution is not flat; however by making a cut on the M_{ee} distribution (c), the resulting $E_{e_1} + E_{e_2}$ distribution (d) is relatively flat.

we will need to do this for the Point 3 $\tilde{\chi}_2^0$ mass measurement, since the cross section is so low—56 fb—so we won't be able to get good results from slicing on invariant mass.]

3 Variations on the endpoint method

The endpoint method suffers from a number of problems. First of all, event selection cuts may bias the endpoints or modify the shape of the energy distribution so that it is no longer flat. Backgrounds may also distort the endpoints.

Secondly, only those electrons that have energies near E_{min} or E_{max} contribute to the fit; the bulk of the electrons which are in the center of the distribution have no effect. The following two methods attempt to take into account the energies of the electrons on both sides of the event simultaneously.

3.1 Endpoint method with extreme energy differences

This method is probably an example of how not to perform this measurement, for reasons that will soon become clear.

The decays of the two sides of the event are independent, so the energies of the electrons are uncorrelated. Some fraction of the time, you would expect that $e_1 \approx E_{min}$ and $e_2 \approx E_{max}$; we can use these events to approximate the endpoints of the distribution.

On an event-by-event basis, we calculate the quantities $M^*_{\tilde{\chi}^0_1}$ and $M^*_{\tilde{e}_R}$ by substituting $E_{min} = e_1$ and $E_{max} = e_2$ into Equations 6. Figure 5 shows the results. $M^*_{\tilde{e}_R}$ peaks at the beam energy (b), but the lower endpoint of the distribution approaches the true $\tilde{e}^\pm_R$ mass (c). As can be seen in (a), $M^*_{\tilde{\chi}^0_1}$ peaks at large masses; only if we take $M^*_{\tilde{e}_R} \approx M_{\tilde{e}_R}$ will the $M^*_{\tilde{\chi}^0_1}$ distribution be close to the true value of $M_{\tilde{\chi}^0_1}$.

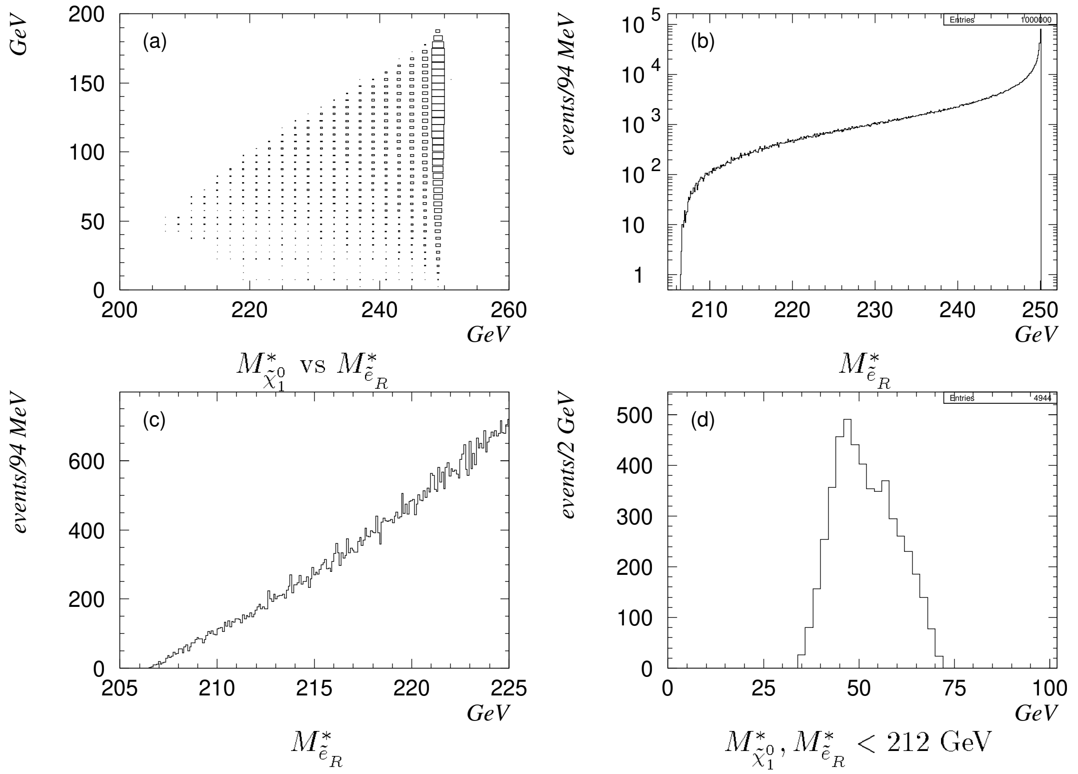

Figure 5: Results from a generator-level simulation of 10^6 events. (a) The distribution of $M^*_{\tilde{\chi}^0_1}$ versus $M^*_{\tilde{e}_R}$. (b) The distribution of $M^*_{\tilde{e}_R}$. (c) A blowup of the $M^*_{\tilde{e}_R}$ plot for regions of small $M^*_{\tilde{e}_R}$. The endpoint of this distribution should be the true $M_{\tilde{e}_R}$. (d) The distribution of $M^*_{\tilde{\chi}^0_1}$ for low values of $M^*_{\tilde{e}_R}$. The peak is around the true value of $M_{\tilde{\chi}^0_1}$.

Although this method does try to use the information on both sides of the event, it is only powerful for an extremely rare set of events: those that have a minimum energy electron in one hemisphere and a maximum energy electron in the other hemisphere. It thus requires very large amounts of data in order to determine the endpoint of the $M^*_{\tilde{e}_R}$ spectrum accurately; backgrounds may also hide the endpoint of the distribution.

3.2 Combining the electron energies

In this section we note that if we randomly take two samples, e_1 and e_2 from a distribution which is uniform between E_{min} and E_{max}, then $e_1 + e_2$ will have a triangle shape distributed between $2E_{min}$ and $2E_{max}$, with a peak at $E_{min} + E_{max}$ and the difference $|e_1 - e_2|$ will have a wedge distribution between zero and $E_{max} - E_{min}$. Figure 6 shows the distributions of these quantities for a generator-level simulation.

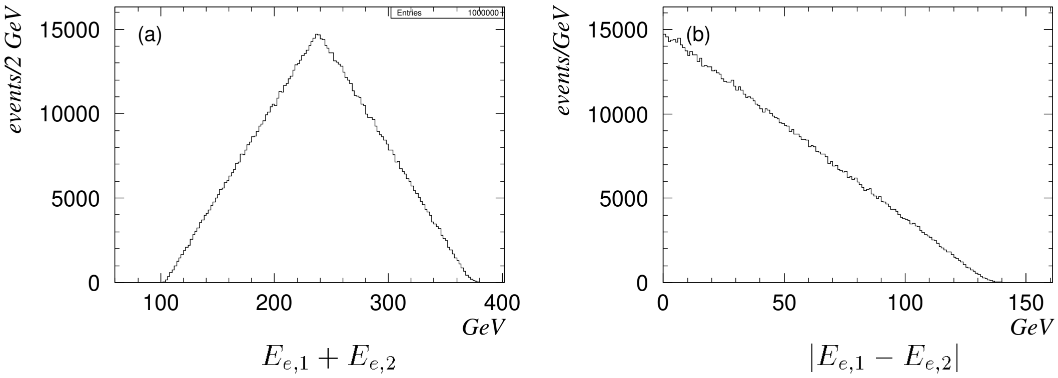

Figure 6: Results from a generator-level simulation of 10^6 events. (a) The sum of the electron energies, with endpoints at $2E_{min}$ and $2E_{max}$ and a peak at $E_{min} + E_{max}$. (b) The difference between the electron energies, with an endpoint at $E_{max} - E_{min}$. The detector resolution is included in these events.

Figure 7 shows the results for 25 fb^{-1} of ISAJET events. The behavior is still pronounced even with the background. It might be interesting to try a $\cos\theta$ cut to reduce standard model background, or an E_{min} or E_{max} cut to reduce the SUSY background.

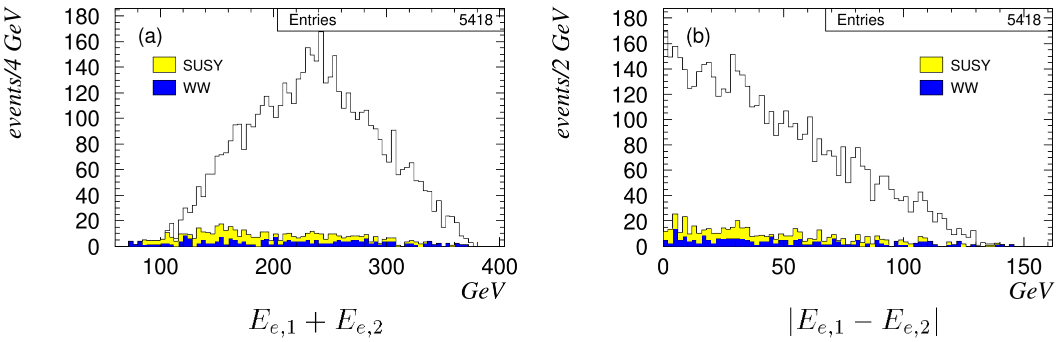

Figure 7: Results from 25 fb^{-1} of ISAJET events. The contributions due to other SUSY processes and standard model backgrounds are also shown.

[Still to do: actually do a fit to the distribution and see if there is any improvement over the endpoint method.]

This may have a slight advantage over the normal endpoint method, in that it is possible to fit to the distributions and extrapolate to points where there is little data. It may also need slightly less data in order for this method to do its work.

There is additional information in the event that is not being used; in particular, we know that the original particles must have equal energy and opposite momenta in the lab frame. We can use this information to provide constraints on the particles masses.

4 Momentum correlations

This analysis is based on one by Feng and Finnell (hep-ph/9310211) on squark masses. Figure 8 shows the production and decay of a $\tilde{e}_R^+\tilde{e}_R^-$ pair. The electrons are the only observed particles, so (using the numbering of this figure) we can measure the energy and momentum of the electrons, e_4, $\mathbf{p}_4$, e_6, $\mathbf{p}_6$, and we define the total visible momentum to be $\mathbf{p}_{vis} = \mathbf{p}_4 + \mathbf{p}_6$. We also know the energy of the original selectrons, $e_1 = e_2 = e_{beam}$.

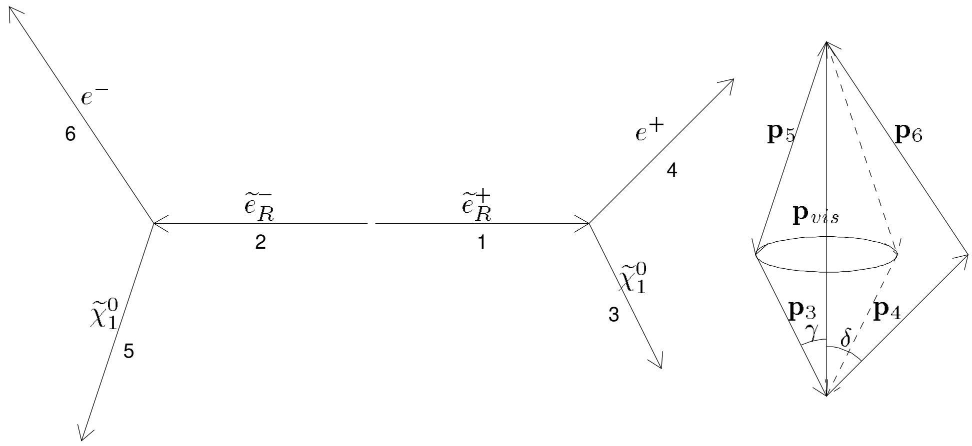

Figure 8: The production and decay of $e^+e^- \to \tilde{e}_R^+\tilde{e}_R^- \to \tilde{\chi}_1^0 e^+ \tilde{\chi}_1^0 e^-$. We label the particles $1\ldots6$. Only $\mathbf{p}_4$ and $\mathbf{p}_6$ are observed, but the figure on the right shows that $\mathbf{p}_{vis} = \mathbf{p}_4 + \mathbf{p}_6 = -(\mathbf{p}_3 + \mathbf{p}_5)$. If the $\tilde{\chi}_1^0$ mass is known, then the momenta $\mathbf{p}_5$ and $-\mathbf{p}_3$ are constrained to lie on the indicated circle.

If we know the mass of the $\tilde{\chi}_1^0$ from previous measurements (say, from the decay of the $\tilde{\chi}_1^\pm$), then we know the magnitudes (but not the directions) of the momenta of the neutralinos:

$$\begin{aligned} p_3 &= \sqrt{e_3^2 - M_{\tilde{\chi}_1^0}^2} \\ &= \sqrt{(e_{beam} - e_4)^2 - M_{\tilde{\chi}_1^0}^2} \end{aligned}$$

The vectors $\mathbf{p}_5$ and $-\mathbf{p}_3$ are required to lie on the circle shown in Figure 8.

We then calculate the minimum kinematically allowed mass and determine the angles γ and δ. The mass is minimum when $\mathbf{p}_1$ is maximum, or when the angle between $\mathbf{p}_3$

and $\mathbf{p}_4$ is maximum and equal to $\gamma + \delta$. Then:

$$\begin{aligned}(M^{min}_{\tilde{e}_R})^2 &= E^2_{beam} - (p^{max}_1)^2 \\ &= E^2_{beam} - p_3^2 - p_4^2 + 2p_3p_4\cos(\gamma+\delta)\end{aligned} \tag{8}$$

where

$$\begin{aligned}\delta &= \cos^{-1}\left(\frac{\mathbf{p}_{vis}\cdot\mathbf{p}_4}{p_{vis}\,p_4}\right) \\ \gamma &= \cos^{-1}\left(\frac{p_3^2+p_{vis}^2-p_5^2}{2p_3\,p_{vis}}\right)\end{aligned}$$

Figure 9 shows the results of the measurement of $M^{min}_{\tilde{e}_R}$ for 10^6 events. Even with no cuts applied, the distribution peaks at the true value of of $M_{\tilde{e}_R}$ (b). SUSY events tend to have large transverse momentum (c), and the effect is enhanced for events that have large p_T (d).

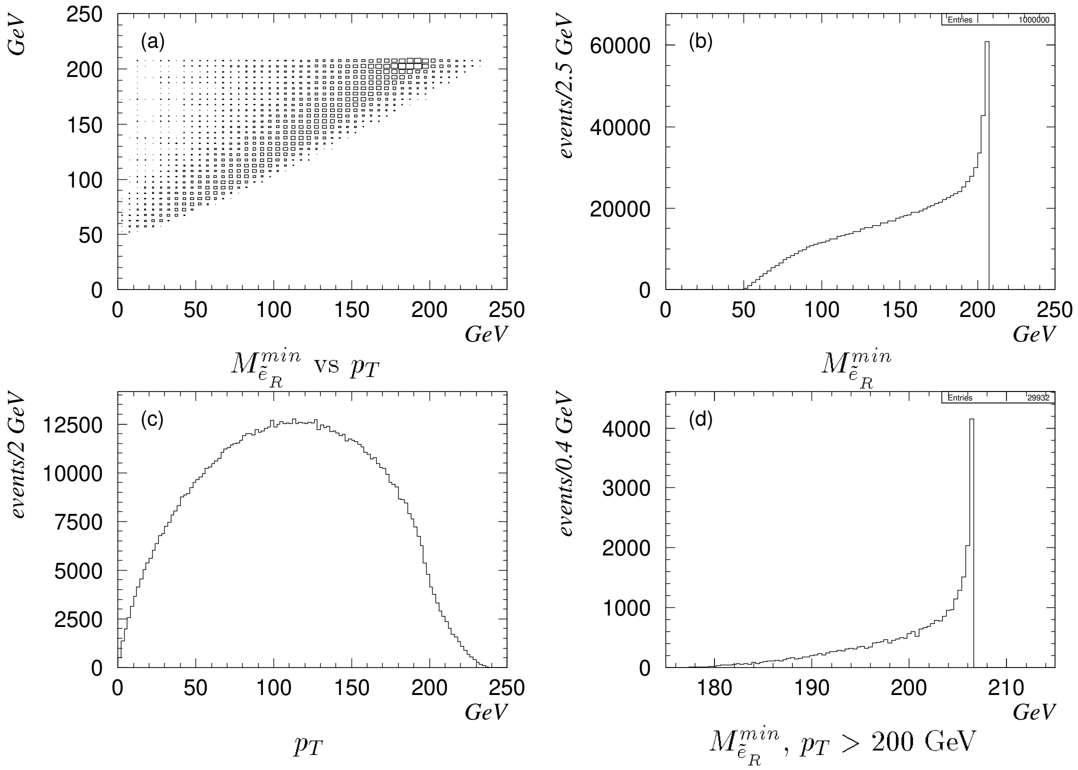

Figure 9: Results from a generator-level simulation of 10^6 events. (a) The distribution of $M^{min}_{\tilde{e}_R}$ vs p_T. (b) The distribution of $M^{min}_{\tilde{e}_R}$ for all events, showing that $M^{min}_{\tilde{e}_R}$ peaks at the true value of $M_{\tilde{e}_R}$. (c) The distribution of p_T for all events. (d) Selecting those events with large p_T enhances the peak in the $M^{min}_{\tilde{e}_R}$ distribution.

[The p_T cut is historical, based on Feng's paper. Transverse momentum is probably a reasonable quantity to cut on at a hadron collider where you don't know p_z of the colliding quarks, but at the NLC we probably want to cut on the magnitude of the total visible momentum, $|\mathbf{p}_{vis}|$.]

In the ISAJET data, we require that there be exactly two electrons in the final state, and no other activity in the detector. Figure 10 shows the results from ISAJET data. As can be seen, a measurement to about 1 GeV or better can be performed. The background is virtually eliminated after a p_T cut (b).

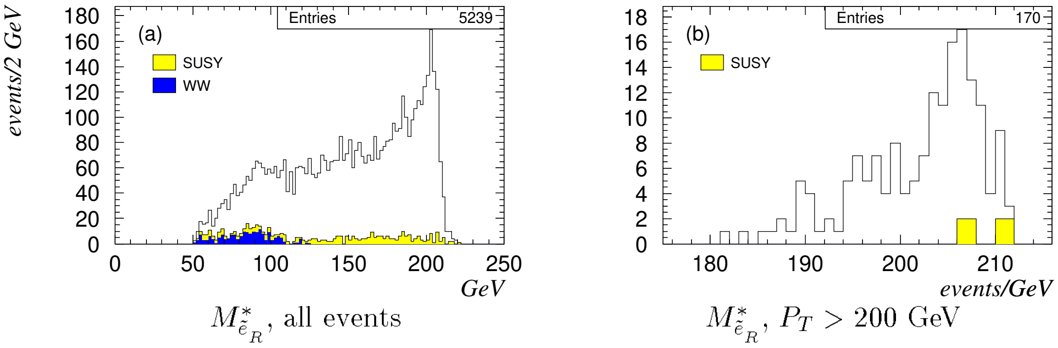

Figure 10: The $M^*_{\tilde{e}_R}$ distributions from ISAJET data (a) for all events satisfying the basic cuts, and (b) only those events passing the p_T cut, including W-pair and SUSY backgrounds.

Feng and Finnell have used this method in a study of squark masses. Figure 11 shows the distribution of $m_{\tilde{q}}^m in$ for both left- and right-handed electron polarization, clearly showing peaks at the left- and right-handed squark masses.

In their study, they find that the statistical error on their mass measurement is 0.5 GeV (0.25%). However, the results are dependent on a good $M_{\tilde{\chi}^0_1}$ mass; a mismeasurement of 1 GeV in $M_{\tilde{\chi}^0_1}$ yields a 1.5 GeV mismeasurement in $M_{\tilde{e}^\pm_R}$.

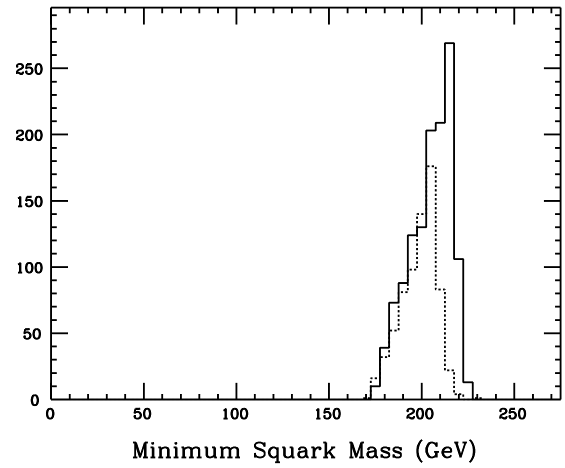

Figure 11: The distribution of $m_{\tilde{q}}^{min}$, the minimum allowed squark mass for a given event. The distribution for e_L^- (e_R^-) is given by the solid (dashed) histogram and is sharply peaked at the actual $\tilde{q}_L$ ($\tilde{q}_R$) mass of 220 (210) GeV.